

# Impact of Zirconia Slurry Doping on 316L Stainless Steel prepared by Laser Powder Bed Fusion for biological/high corrosion applications

McKay Sperry\*, Jakob Bates\*, Taylor Davis\*, Tracy W. Nelson\*, Nathan B. Crane\*

\*Brigham Young University, Provo, UT, USA

## Abstract

Laser Powder Bed Fusion (LPBF) is a versatile additive manufacturing (AM) method used primarily for processing plastics and metals. Stainless steel (type 316L) is a biocompatible metal used extensively for LPBF and commonly for medical applications. Zirconium Dioxide (zirconia) is a common engineering material used in applications ranging from dental implants to oxide dispersion strengthening of metals. This paper presents the process development and results of in-situ deposition of small quantities of zirconia nanoparticles in a stainless steel (316L) powder bed prior to fusion in the LPBF process. The zirconia slurry was deposited as an atomized mist. The deposition process may be adapted to selectively dope a powder bed to form parts with spatially varying properties for use in complex parts. In this work, the added zirconia was shown to be partially distributed in the matrix, but a large portion segregated to grain boundaries and surfaces. Porosity increased in multi-layer parts with the zirconia agglomerated on the porous surfaces. This is undesirable for many applications but may be useful for creating porous surfaces for heat exchanger or bio-integration applications. The deposition of zirconia limits the anisotropic crystal growth throughout the entire doped region.

Key words: Laser Powder Bed Fusion, Stainless Steel 316L, Zirconia

## Introduction

Additive Manufacturing (AM), often informally called 3D printing, is attractive to many specialized industries because it is suitable for complex geometry and customized or low volume production [1]. Traditionally, highly sophisticated cutting machines and tools have been used to produce small batches of specialized devices for industries ranging from medicine to aviation [2]. Machining biocompatible metals such as titanium alloys and stainless steel 316L is especially difficult due to work hardening and resulting negative effects on tools and finished products [3]. AM processes, however, allow for cost-effective mass customization by eliminating part-specific tooling. Engineers can also utilize the increased design flexibility of AM to combine multiple parts into single assemblies in a practice called functionality integration [4].

Functionally integrated parts can save time and resources by simplifying processing and assembly, reducing material waste, and minimizing weight [5]. A prominent example of functionality integration is a dental strut implant, where an abutment and strut are built as a single part with Laser Powder Bed Fusion (LPBF) [6]. In this single part, the lower portion must be compatible with bone, while the upper portion must be compatible with human gums. This example highlights one of the greatest challenges of functionality integration. Multi-component

assemblies frequently require different properties in different parts of the assembly. The dental implant design works well because the property change is only required in one direction. However, functionally integrated designs are much more difficult to execute when an assembly requires different properties in three dimensions [7-9].

To overcome this, AM processes need increased spatial control of properties. Powder Bed Fusion (PBF) is a family of AM processes wherein complex and detailed parts can be built by spreading a thin layer of powder, then fusing a specific cross section of the powder. This process can be repeated thousands of times for large parts. The powders used for PBF include plastics, ceramics, composites, and metals, many of which are engineered for biocompatibility [10-13]. The most common method for metal PBF is LPBF, where the powder is melted by a laser. Binder Jetting (BJ), an alternative to PBF, uses high precision ink jet printing to introduce binding agents to thin layers of powder to form a loosely bound structure, after which this green part is sintered in a furnace [14]. LPBF and BJ both have specific advantages. LPBF can form precise parts without shrinkage and limited need for post-processing. BJ can introduce secondary materials to the part to aid in post-processing or performance [1, 15]. A LPBF process that borrows the principle of adding a second material to a powder bed from BJ could make 3-dimensional property manipulation an additional element in the design space of engineers in specialized fields.

One of the greatest challenges of changing the properties of parts is choosing secondary materials that can achieve useful property changes with small composition changes [16]. Low carbon stainless steel is a noteworthy material for this study due to its biocompatibility and sensitivity to small changes in composition [17]. Stainless steels are common iron-based alloys that contain chromium and nickel. Carbon and other elements are also frequently added to increase hardness, ductility, and other properties [18].

Control of properties and materials is an area of great importance in both AM and biomedical engineering as illustrated by the example given of a dental strut implant. There are many methods available to change properties with small composition changes while maintaining biocompatibility [8, 12, 16, 19-22]. Alloying, carbiding, and oxide dispersion are common methods to modify the properties of metal and have all been used with LPBF. AlMangour et al. increased the yield strength of stainless steel (316L) prepared with LPBF by approximately 35% by pre-mixing steel powder with titanium carbide particles using a ball milling process [23]. This increase in strength is impressive. However, the addition of carbide by this method is time consuming and requires that the entire part be built of the modified material, which would be detrimental if hardness or some property other than strength is required [24].

Another notable attempt to modify the properties of LPBF parts uses a high precision vacuum and dispenser system to remove the base material and insert a secondary material in specified locations [7]. Full parts composed of both stainless steel (316L) and copper alloy (Cu10Sn) were built by this method, with each material exhibiting unique properties. This method approaches the flexibility in materials of directed energy deposition (DED), where streams of any material can be directed in front of a high-powered beam and mixed by melting, but with the enhanced environmental control and resolution of LPBF [25, 26]. However, the cost in added fabrication time for multi-powder deposition is significant [15]. Additionally, depositing the secondary material in this way alters the powder packing, resulting in unpredictable pores, cracks, and other defects where the second material is added [7].

Oxide Dispersion Strengthened (ODS) Steels are a sub-class of iron-based nanocomposite materials with enhanced properties [27, 28]. ODS parts are typically fabricated from pre-mixed steel/oxide powders and have been processed with LPBF using similar methods to AlMangour, yielding similar results, with similar pitfalls [29, 30]. However, multiple studies show that off-the-shelf oxide nanoparticles can be deposited on a steel powder bed using inkjet technology. Davis has explored the influence of various concentrations of Zirconium Oxide (zirconia) on print parameters using single track scans, while Paul demonstrated that yttria nanoparticles deposited on the powder surface can be integrated into the steel matrix, although with some negative affects including porosity due to organic carriers used for deposition [31, 32].

This work explores the effects of introducing small quantities ( $\leq 1$  wt%) of zirconia nanoparticles into stainless steel (SS 316L) during the LPBF process for multi-layer specimens to form nanocomposites of biocompatible materials. This study will evaluate the effectiveness of the convective fluid motion in PBF melt pools to disperse zirconia in the metal matrix. Partial re-melting of lower layers in multi-layer specimens is expected to increase oxide mixing [33]. Additionally, this work will explore the quality of zirconia dispersion in the stainless steel and the impact on the resulting part structure. The change in hardness and the crystalline structure will be compared with unmodified LPBF SS316L. This is the first time that the process will be applied to multi-layer parts.

## Methods

### Materials and Processing

A Concept Laser M2 Cusing dual laser Direct Metal Laser Sintering (DMLS, LPBF) machine was used to form all parts for this study. Three sets of standard laser processing parameters were used to form both single layer and eight-layer rectangular specimens. The standard upskin, downskin, and bulk parameters were used because they have demonstrated good properties for general applications. The specifications for each set of processing parameters include laser spot size, laser scan speed, and laser power (see Table 1). These variables combine to give the energy density, an important factor in predicting part performance. Energy density can be defined in different ways, but for this study a common expression for areal energy density is given by

$$ED_a = P_A t_d = \left(\frac{P}{A_s}\right) \left(\frac{d_b}{v}\right) = \frac{P}{v d_b} \left(\frac{4}{\pi}\right) \quad [1]$$

where P is power,  $t_d$  is the exposure time, A is the area covered by the laser, d is laser diameter, v is laser speed. Additionally, 44 single line scans were performed using various input parameters, found in Appendix A. Single line scans provide valuable information relative to the flow of molten material and can be used to predict appropriate inputs for full parts [34]. The ambient atmosphere is nitrogen, with an oxygen content no greater than 0.2%.

Table 1. Laser input parameters used for area and multi-layer parts.

Parameter	Spot Size ( $\mu\text{m}$ )	Scan Speed (mm/s)	Laser Power (W)	Areal Energy Density ( $\text{J}/\text{mm}^2$ )
Upskin (US)	130	980	200	1.570
Downskin (DS)	130	1350	280	1.595
Bulk (BP)	130	1350	370	2.108

The purpose of this paper is to observe the impact of a zirconia slurry deposited onto a stainless steel powder bed between layers of LPBF process and its impact on the resulting microstructure, composition, and microhardness. The zirconia slurry (NYACOL Nanotechnologies Inc.) is a 20 wt% suspension of 100 nm zirconia particles in water with no other additives. The powder is a 316L stainless steel powder from Concept Laser (CL 20ES) with mean particle size of 45  $\mu\text{m}$ .

This study is primarily concerned with 2D and 2.5D (extrusions of 2D geometries) parts with uniform doping. Rather than utilize inkjet printing deposition [31, 32], a piezoelectric atomizer (mister) was used to create a mist of fine droplets, allowing for a greatly simplified deposition process. The mister allows for doping between 3 and 10 mm in a single pass, depending on the distance from the substrate. It forms droplets that spread over a wide area with a relatively uniform distribution, while an inkjet printhead requires precise -x and -y direction controls to cover a similar area, one line at a time (see Figure 1).

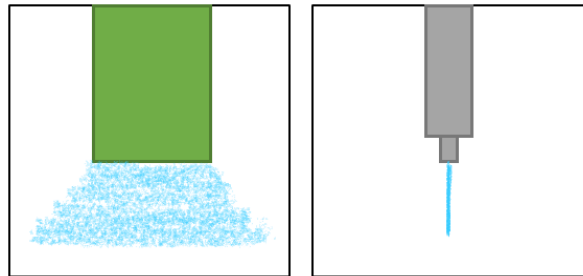


Figure 1. Large area deposition mode of piezoelectric mister (left) vs small area deposition of inkjet printhead (right).

Zirconia deposition was measured by misting onto 5mm x 20mm strips of plastic shim material of known weight. The misting device was attached to a 3-axis stage and moved over a carefully arranged array of shim strips at a constant speed. After drying, the shim strips were weighed to determine the quantity of zirconia deposited per unit area. The speed at which the device moved over the test area was adjusted until deposition mass was equivalent to 1 wt% of a 0.05 mm thick layer of SS316L in the main column of mist (see Figure 1). The amount of deposited zirconia outside of the central 5 mm below the column of mist was negligibly small.

A misting module was designed to integrate with the coater blade of the LPBF machine. A microcontroller was used to precisely trigger zirconia deposition only in the area of interest to avoid contaminating surrounding powder. This simple setup allowed for zirconia deposition in the x direction with the movement of the coater blade, and the z direction with the movement of the build plate.

The build plate was heated to 70 °C to aid in drying the water from the zirconia slurry. The LPBF machine was allowed to spread standard layers of 0.05 mm with the misting device depositing zirconia directly after each layer was spread. The process was manually paused for 5 minutes after each layer to ensure that all water had evaporated from the build area, which could cause severe denudation as rapidly expanding water vapor explosively pushed unfused powder away from the laser [35]. The basic process is depicted in Figure 2. Undoped samples were formed with the same laser parameters in parallel to the zirconia doped samples for direct comparison.

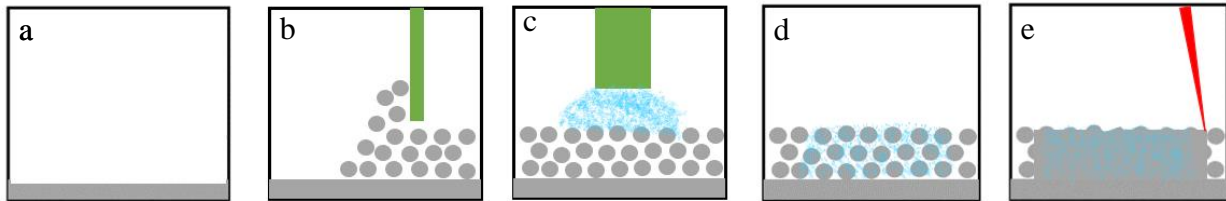


Figure 2. Experimental approach for introduction of zirconia into steel powder bed. a) a flat substrate is prepared to receive a layer of fresh powder. b) A thin layer of powder is spread over the build area by a coater blade. c) The misting device deposits zirconia into the build area directly after fresh powder is spread. d) The powder bed is left to sit for 5 minutes to allow all residual water to evaporate. e) A laser melts the powder, trapping zirconia in the solidified metal matrix.

### Measurement and Characterization

After laser fusion, the samples were removed from the LPBF machine and cleaned carefully with a toothbrush to remove excess powder. Roughness was measured optically by a Keyence VHX-7000 microscope. The samples were then sectioned via waterjet to obtain a cross-section view of the region where zirconia was deposited. Next, the samples were fixed in a clear epoxy resin and polished to a mirror finish, with 0.05  $\mu\text{m}$  silica vibrational polishing as the final step.

The distribution of zirconia in the steel was determined by Energy Dispersive X-ray Spectroscopy (EDS) using a Verios G4 UC Scanning Electron Microscope. Vickers hardness was measured by a Leco LM100AT microhardness tester conforming to ASTM standard E92-17 with a force of 200 N. Hardness was only measured for the 8-layer samples, where a sufficiently thick layer of steel was fused to the substrate to make hardness indentations. Twenty hardness indentations were performed on each sample in the doped region and at a corresponding location on the undoped samples.

The samples were then etched electrolytically in a 10% Oxalic acid solution to expose the microstructure. Optical imaging was performed with the same Keyence microscope used to measure roughness. The image processing software ImageJ [36] was used to analyze these images to measure melt pool dimensions of the single line scans (Figure 3) and determine porosity of the multi-layer parts (Figure 9).

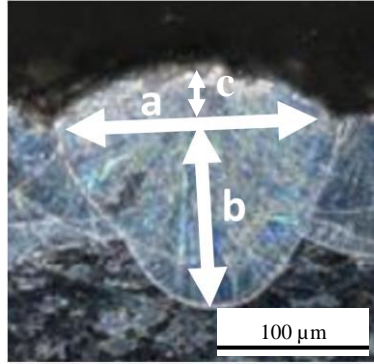


Figure 3. Typical cross section of etched single line melt pool formed with LPBF. The key dimensions of width at the surface plane (a), depth from the surface plane (b), and height from the surface plane (c) are shown.

The single line scans were classified by researchers familiar with, but not closely involved in this work using the classification categories illustrated in Figure 4 as a guide.



Figure 4. Example single line scans used to aid volunteers in classifying melt pools. Class 5) Continuous melt pool. Class 4) Nearly continuous with some balling. Class 3) Balling across entire scan. Class 2) Balling with some unfused gaps between balls. Class 1) Mostly unfused, but with some balling present.

## Results and Discussion

### Single Line Scans

Balling is a common defect in LPBF, which can be observed in single line scans. Single line scans with an aerial energy density less than  $2.5 \text{ J/mm}^2$  were nearly all within the balling regime, as shown in Figure 5. The addition of 1 wt% zirconia slightly decreased the energy required to achieve continuous or nearly continuous lines. The slight change may be due to the zirconia decreasing the reflectivity of the steel powder, allowing more energy to be absorbed. This supports the findings of Davis, and indicates that the addition of zirconia has little impact on the melt pool-substrate interaction for single lines [31].

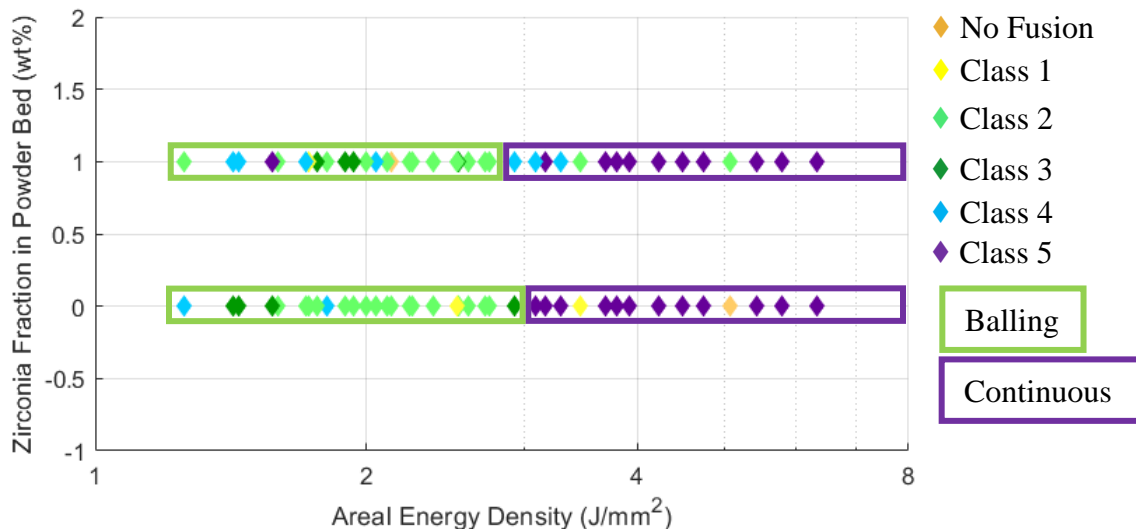


Figure 5. Influence of zirconia on single line fidelity for various energy density inputs. Class 1 includes samples with minimal fusion, and balling where fusion occurs. Class 2 includes samples with increased fusion, but large gaps between balls. Class 3 includes full balling with minimal gaps between balls. Class 4 includes nearly continuous melt pools with some balling. Class 5 includes fully continuous melt pools without balling. The continuous and balling regimes are highlighted by colored boxes corresponding to their respective marker colors.

Melt pool provides an additional measure of the impact of zirconia on the powder processing characteristics. Melt pool geometries are not easily measured in the balling regime, so only continuous and nearly continuous single line scans were measured. The addition of zirconia generally increased the predictability of melt pool width and depth, as shown in Figure 6, with no significant trends in height from the surface plane compared to undoped melt pools. In contrast, Davis showed an increased melt pool height from the surface plane with the addition of zirconia [31]. This may be because Davis used inkjet printing of large quantities of dopant and much larger zirconia quantities. These differences may have increased the surface zirconia levels more than the misting methods used here. Both deposition method and concentration could change the laser absorptivity and affinity of zirconia to segregate. In general, melt pool width and depth both increased as energy density increased. This was expected and is supported by the literature [34, 37]. The data contained in Figure 5 and Figure 6 corresponds to similar figures by Davis, and is intended to expand the data sets presented in that work [31].

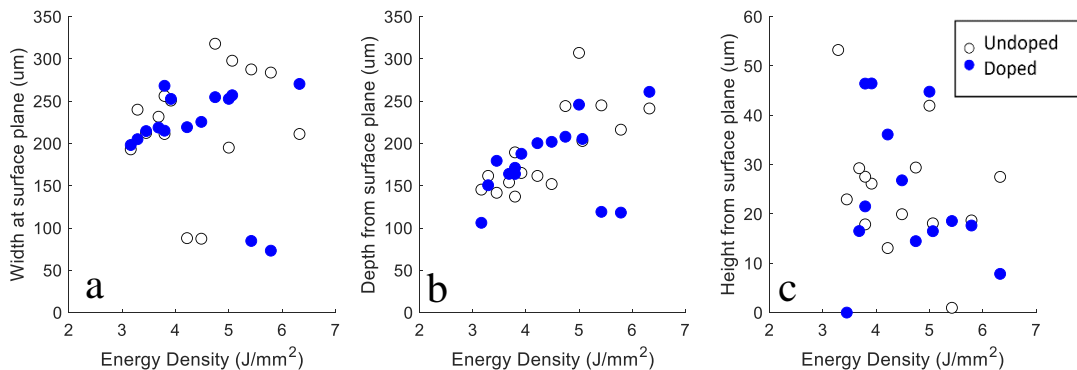


Figure 6. Width, depth, and height of single line melt pools. Plots a, b, and c correspond to dimensions a, b, and c of Figure 3.

## Roughness

The area roughness of the undoped samples was comparable to literature reports of samples prepared independently with similar inputs [38]. In general, roughness increased significantly for the zirconia doped parts. Figure 7 shows a characteristic example from of undoped (a) and zirconia doped (b) samples and the mean roughness of all 16 samples.

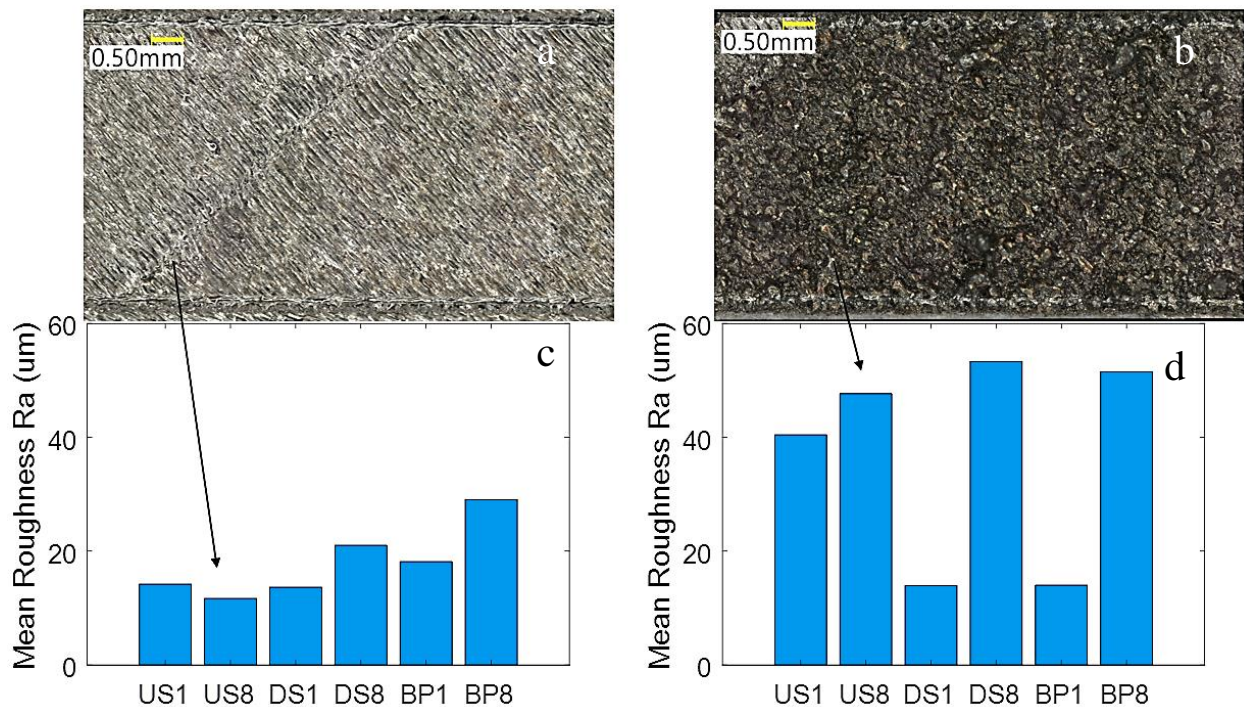


Figure 7. Undoped (left) and zirconia doped (right) area roughness for single layer upskin parameter scan (US1), 8 layer upskin scan (US8), single layer downskin parameter scan (DS1), 8 layer downskin scan (DS8), single layer bulk parameters (BP1), 8 layer bulk parameters (BP8). Characteristic images of the undoped US8 sample and the doped US8 sample are shown. All multi-layer samples have similar appearance.

The exceptions to the trend of increased roughness are the single layer downskin and bulk parameter scans, where roughness decreased with zirconia doping. For these areas, it was impossible to clean all the residual zirconia from the surface prior to taking measurements. This residual zirconia likely filled in the deepest cervices, resulting in a smoother surface, but preventing a true measurement of the roughness of only the fused material (Figure 8). To maintain consistency, the roughness of the entire doped region was measured. But a more accurate roughness measurement of only the fused material may have been achieved by more forceful cleaning or by manually measuring regions without agglomerated zirconia and unfused stainless steel powder on the surface.

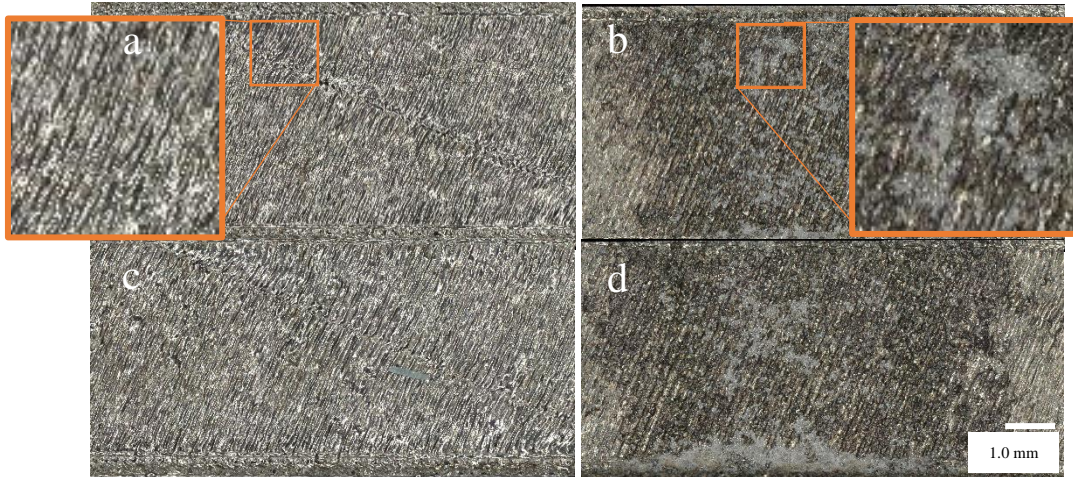


Figure 8. Top view of single layer scans. a) downskin parameters (DS1) without zirconia. b) downskin parameters (DS1) with zirconia doping. c) bulk parameters (PB1) without zirconia. d) bulk parameters (PB1) with zirconia doping. The lighter grey areas in b) and d) are agglomerated zirconia and steel adhered to the surface.

## Porosity

LPBF can produce parts with near 100% density and good surface finish on exterior surfaces under normal conditions [39]. This holds true for the control group in this study as seen in Figure 9. There was zero porosity measured in any of the control specimens. There was also negligible porosity in the single-layer specimens with zirconia doping. When zirconia was added to multi-layer parts, however, porosity increased to around 12%, with some regions exhibiting up to 30% (Figure 9). The pores are long and nearly continuous. Similar pores exist in the 8-layer samples with zirconia under all tested process parameters.

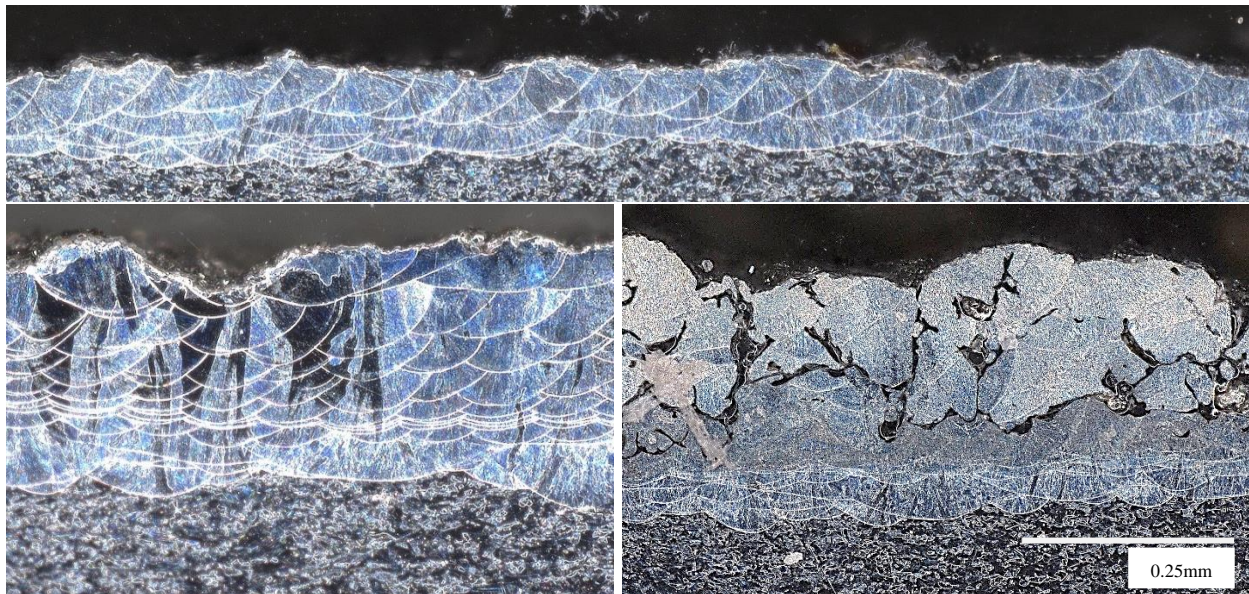


Figure 9. Zirconia-doped Single layer SS316L specimen with no measurable porosity (top), Undoped 8-layer SS316L test specimen (bottom left), and 8-layer SS316L test specimen with 1 wt% zirconia deposited by the misting technique described for this study (bottom right). All samples etched to reveal grain structure.

## Composition (EDX)

EDX reveals that most of the zirconia agglomerated near porous surfaces within the multi-layer specimens. In Figure 10c, the contrast in the image shows differing atomic weights, where the lightest grey regions are primarily zirconium in the zirconia, the darker grey is primarily iron in the steel, and the black is primarily carbon in the epoxy. The height of the zirconium peak relative to other peaks in the EDX data (Figure 10a and Figure 10b) indicates the relative quantity of zirconia in the region of interest. Several factors may play into the segregation of zirconia from the stainless steel, and the resulting porosity. Particles on the nano scale have extremely high surface energy, surface electrostatic charge, and van der Waals forces due to their high surface area to volume ratio. These high energy, unstable particles can quickly reduce their total free energy by agglomerating, which is likely why most of the zirconia is found clumped together [40].

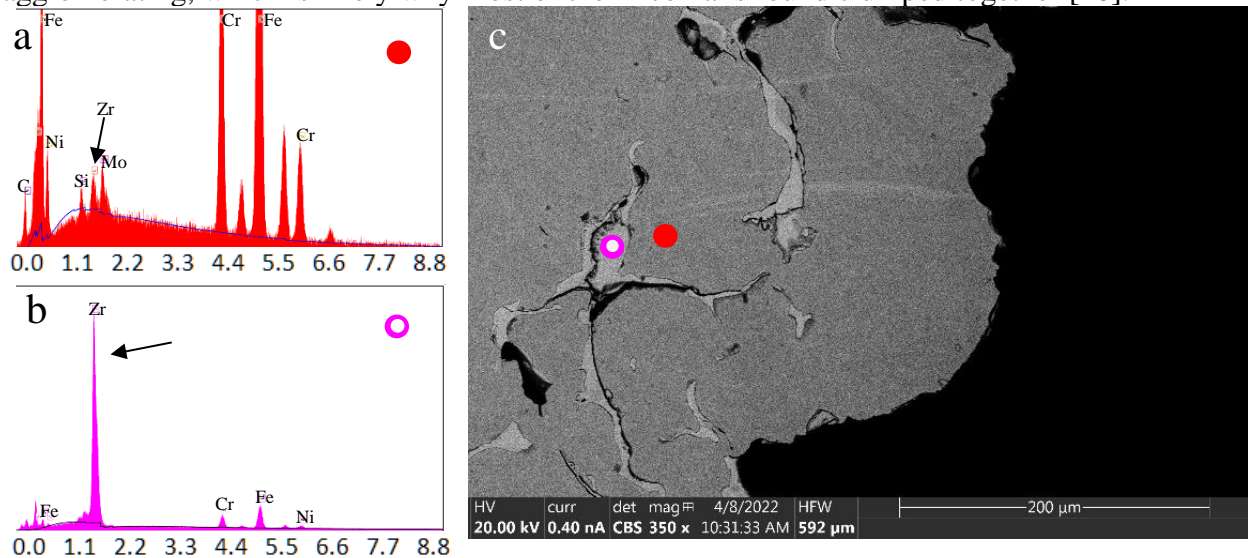


Figure 10. Electron backscatter micrograph with accompanying EDX data. The red and magenta dots on the micrograph indicate the location where the corresponding EDX count was taken. The arrows indicate x-ray peaks associated with zirconium.

Although most of the zirconia agglomerated near pores, Figure 11 indicates that some zirconia dispersed into the stainless steel. Due to the high melting point of zirconia relative to temperatures achieved in this test, it is unlikely that zirconia melted into the stainless steel [41]. Instead, the convective motion of the liquid melt pool likely mixed solid nanoparticles into the bulk stainless steel, resulting in the structure of Figure 11. The concentration is too small to achieve an accurate EDX count. However, the brightness of the circular particles in Figure 11 indicate they primarily consist of an element heavier than iron. Given the composition of SS 316L, it is unlikely that the circular particles are anything other than zirconia. The size is also in the expected range of the zirconia particles on the order of 100 nm.

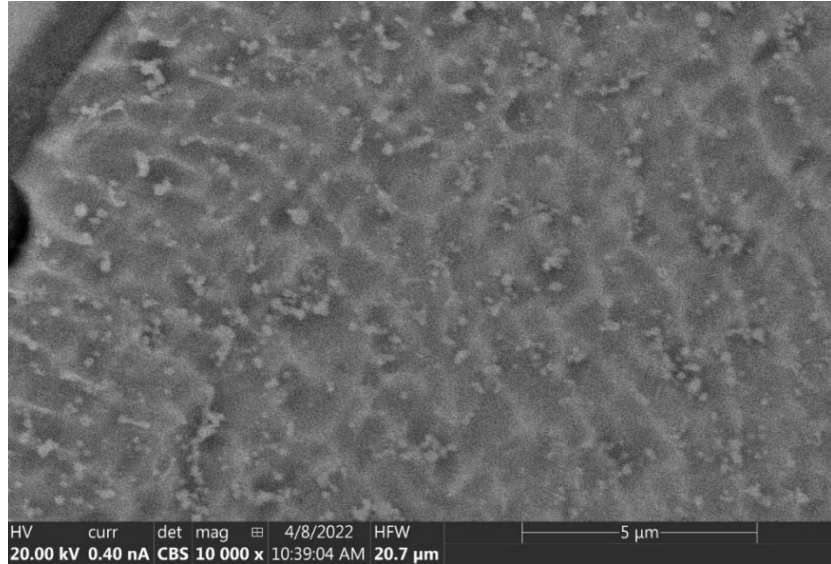


Figure 11. Backscatter SEM image of stainless steel with zirconia doping. Circular inclusions are likely dispersed zirconia.

## Hardness

The doped and undoped samples have considerable overlap in hardness as seen in Figure 12. The median hardness of the zirconia doped samples decreased, likely due to porosity adjacent to or below the indentation, as opposed to the undoped samples where no porosity was observed. With outliers removed, the undoped samples were still an average of 27 points harder than the zirconia doped samples on the Vickers scale. While a decrease in hardness is concerning, the average hardness of the zirconia doped samples is still 100 HV harder than as-annealed SS 316L [17].

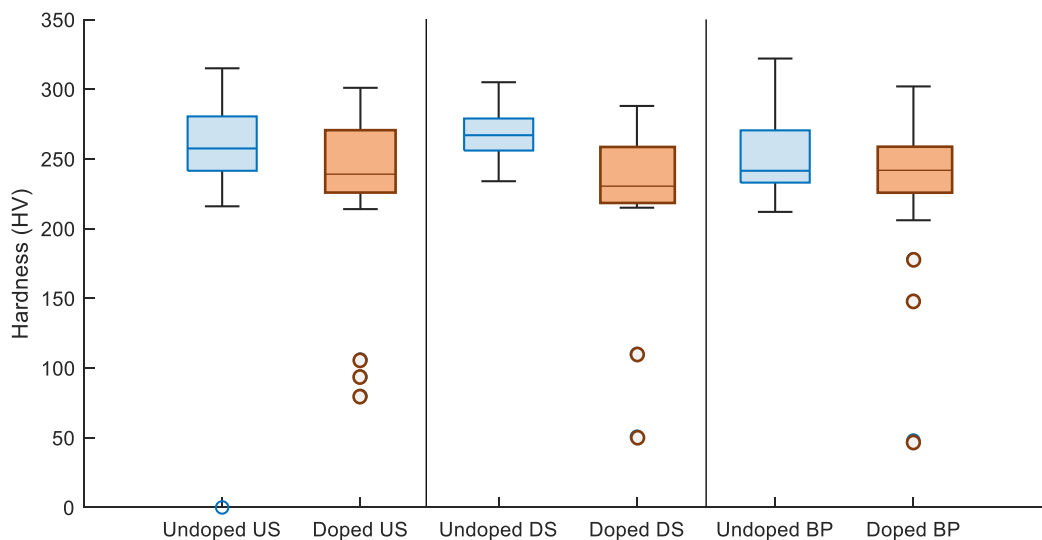


Figure 12. Box and whisker summaries of hardness measurement results. Outliers, 1.5 IQR or further from the lower quartile, are shown by circles. US, DS, and BP correspond to upskin, downskin, and bulk parameters as given in Table 1.

## Crystalline structure

The crystalline structure of the zirconia doped samples is starkly different from that of the undoped samples. In Figure 13a the undoped samples show columnar grains elongated in the

direction of material addition (conventionally the -z direction). In contrast, the zirconia doped specimen shown in Figure 13b shows no pattern of anisotropic grain growth. This may be partially due to pores blocking the growth of crystals. But even away from pores, the anisotropic crystal growth that is characteristic of additive manufacturing is nearly eliminated with the addition of zirconia. This may be caused by enhanced precipitation because of the nanoparticles that mixed into the melt pool [45]. Isotropic crystal growth mitigates anisotropy in properties, one of the main flaws of AM [15].

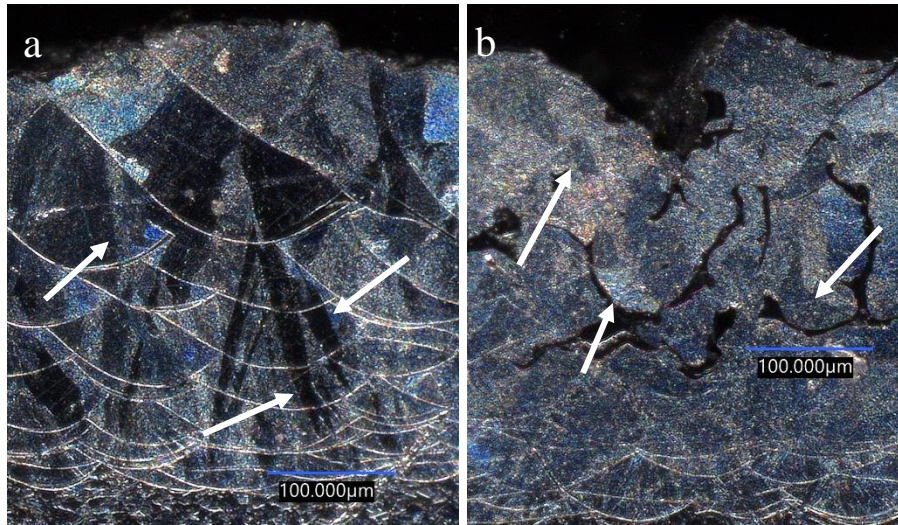


Figure 13. Microstructure in multi-layer stainless steel AM specimens. 10a shows a sample with no dopant. 10b shows a sample with a small amount of zirconia deposited on the surface of each layer. Arrows point to several characteristic grains in each image.

## Conclusions

In this study, small quantities of zirconia nanoparticles were deposited on the surface of a stainless steel 316L powder bed prior to laser fusion in LPBF. The nanoparticles were evenly distributed across the area of interest in a water suspension by a piezoelectric atomizing mister. The area was then fused by a high-powered laser. The fused steel was measured for roughness, then sectioned and polished to measure the influence of zirconia on single line scans, bulk composition and hardness, and to observe the crystal structure.

1. Single line scans indicate that adding small amounts of zirconia does little to change the geometry of the melt pool. There is also a negligible difference between undoped and doped single layer specimens in melt pool size. These results show little influence from the zirconia on the melt pool-substrate interaction. Zirconia in multi-layer parts increased the porosity of the stainless steel. The zirconia mostly agglomerated near the porous interfaces within the stainless steel matrix, similar to the initial results of Paul et al. [32]. However, some zirconia mixed into the stainless steel as shown in Figure 11. Re-melting the zirconia-doped region, as per the method of Yu et al. [33] may increase the amount of mixing due to increased fluid motion. However, further experimentation is required to verify this hypothesis.
2. The average hardness of the 8-layer stainless steel parts decreased slightly with the inclusion of oxide nanoparticles. This contradicts the results of Zhong et al., Yan et al., and Pawawoi et al. [27-29]. The contradiction may be explained by the porous test surface, shown in Figure 9, which reduces the reliability of microhardness testing. A non-porous

test surface may be achieved by changing laser scan parameters, especially increasing areal energy density [39, 46].

3. Although the mechanical properties of the stainless steel were reduced, anisotropy in the crystal structure was nearly eliminated (Figure 13). LPBF generally forms parts with dendritic crystals growing in the direction of material addition. The minimization of dendritic crystals typically results in a stronger, but a less ductile, final product. A similar result is expected for LPBF if full density parts are achieved without dendritic crystal growth. In this case, anisotropic crystal growth was likely reduced due to zirconia nanoparticles serving as nucleation points, making nucleation of new crystals more energetically favorable than growth of existing crystals [45, 47].
4. The porosity of the zirconia-treated samples is a critical limitation for most LPBF applications. However, this may be favorable as a surface treatment in some biological applications. Porosity can be beneficial for osseointegration of implants, and is often a sought-after feature of medical devices, especially those formed with AM [11, 48-50]. The porous surface of Figure 9 resembles the bone scaffold structure of Jiao et al [51], and the porous surface structures of Wu et al [13] and Kwak et al [52] intended for osseointegration. Additionally, zirconia is a biocompatible material that has been shown to behave similarly to other oxides used for ODS strengthening [42], which improve corrosion resistance even in the most extreme environments [53]. Similar results may be observed from incorporating zirconia into other biocompatible metals such as titanium.

## Appendix A: Processing parameters used for single line scans

<b>Line #</b>	<b>Laser Power (W)</b>	<b>Spot Size (um)</b>	<b>Scan speed (mm/s)</b>	<b>Energy Density (J/mm<sup>2</sup>)</b>
<b>1</b>	370	130	450	6.325
<b>2</b>	395	130	525	5.788
<b>3</b>	370	130	525	5.421
<b>4</b>	395	130	600	5.064
<b>5</b>	370	130	600	4.744
<b>6</b>	370	100	825	4.485
<b>7</b>	370	130	675	4.217
<b>8</b>	370	70	1350	3.915
<b>9</b>	370	100	975	3.795
<b>10</b>	370	130	750	3.795
<b>11</b>	395	130	825	3.683
<b>12</b>	370	130	825	3.45
<b>13</b>	370	100	1125	3.289
<b>14</b>	370	130	900	3.162
<b>15</b>	370	100	1200	3.083
<b>16</b>	370	130	975	2.919

<b>17</b>	370	100	1350	2.741
<b>18</b>	370	130	1050	2.711
<b>19</b>	370	100	1425	2.596
<b>20</b>	370	130	1125	2.53
<b>21</b>	340	100	1350	2.519
<b>22</b>	370	130	1200	2.372
<b>23</b>	395	130	1350	2.251
<b>24</b>	370	130	1275	2.232
<b>25</b>	395	130	1425	2.132
<b>26</b>	370	130	1350	2.108
<b>27</b>	340	130	1275	2.051
<b>28</b>	370	130	1425	1.997
<b>29</b>	340	130	1350	1.937
<b>30</b>	370	130	1500	1.897
<b>31</b>	370	130	1575	1.807
<b>32</b>	310	130	1350	1.766
<b>33</b>	370	130	1650	1.725
<b>34</b>	370	160	1350	1.713
<b>35</b>	280	130	1350	1.595
<b>36</b>	340	160	1350	1.574
<b>37</b>	370	190	1350	1.442
<b>38</b>	250	130	1350	1.425
<b>39</b>	220	130	1350	1.254
<b>40</b>	190	130	1350	1.083

## References

1. Brandt, M., *Laser additive manufacturing: Materials, design, technologies, and applications*. Laser Additive Manufacturing: Materials, Design, Technologies, and Applications. 2016: Elsevier Inc. 1-479.
2. Kalpakjian, S., *Manufacturing engineering and technology*. 6th ed. ed, ed. S.R. Schmid. 2010: Prentice Hall, New York.
3. Jackson, M.J. and J.P. Davim, *Medical Device Manufacturing*. 2012, New York, UNITED STATES: Nova Science Publishers, Incorporated.
4. Moritz, J., et al., *Functional integration approaches via laser powder bed processing*. Journal of Laser Applications, 2019. **31**(2).
5. Eliseeva, O.V., et al., *Functionally Graded Materials through robotics-inspired path planning*. Materials & Design, 2019. **182**: p. 107975.
6. Kain, M., et al. *Metal additive manufacturing of multi-material dental strut implants*. in *20th International Conference of the European Society for Precision Engineering and Nanotechnology, EUSPEN 2020, June 8, 2020 - June 12, 2020*. 2020. Geneva, Virtual, Austria: euspen.

7. Wei, C., et al., *3D printing of multiple metallic materials via modified selective laser melting*. CIRP Annals, 2018. **67**(1): p. 245-248.
8. Tammam-Williams, S. and I. Todd, *Design for additive manufacturing with site-specific properties in metals and alloys*. Scripta Materialia, 2017. **135**: p. 105-110.
9. Nadimpalli, V.K., et al. *Multi-material additive manufacturing of steels using laser powder bed fusion*. in *19th International Conference of the European Society for Precision Engineering and Nanotechnology, EUSPEN 2019, June 3, 2019 - June 7, 2019*. 2019. Bilbao, Spain: euspen.
10. Sherman, L.M., *Additive manufacturing: Materials for 'real-world' parts*. Plastics Technology, 2014. **60**(3): p. 42-47.
11. Coffigniez, M., et al., *Direct-ink writing of strong and biocompatible titanium scaffolds with bimodal interconnected porosity*. Additive Manufacturing, 2021. **39**.
12. Heer, B., Y. Zhang, and A. Bandyopadhyay, *Additive manufacturing of alumina-silica reinforced Ti6Al4V for articulating surfaces of load-bearing implants*. Ceramics International, 2021. **47**(13): p. 18875-18885.
13. Wu, Y., et al., *A Critical Review of Additive Manufacturing Techniques and Associated Biomaterials Used in Bone Tissue Engineering*. Polymers, 2022. **14**(10).
14. Ziaee, M. and N.B. Crane, *Binder jetting: A review of process, materials, and methods*. Additive Manufacturing, 2019. **28**: p. 781-801.
15. Sun, S., M. Brandt, and M. Easton, *Powder bed fusion processes: An overview*. 2017, Elsevier Inc. p. 55-77.
16. Binder, M., et al. *Potentials and challenges of multi-material processing by laser-based powder bed fusion*. in *29th Annual International Solid Freeform Fabrication Symposium - An Additive Manufacturing Conference, SFF 2018, August 13, 2018 - August 15, 2018*. 2020. Austin, TX, United states: The University of Texas at Austin.
17. Lula, R.A., *Stainless steel*, ed. J.G. Parr. 1986: American Society for Metals, Metals Park, Ohio.
18. Gladman, T., *The physical metallurgy of microalloyed steels*. Book / The Institute of Materials. 2002, London: Maney. 363.
19. Anand, M. and A.K. Das, *Issues in fabrication of 3D components through DMLS Technique: A review*. Optics & Laser Technology, 2021. **139**: p. 106914.
20. Brueckner, F., et al., *Enhanced manufacturing possibilities using multi-materials: In laser metal deposition*. LIA Today, 2018. **26**(2): p. 10-12.
21. *Medical Devices*. 1st edition 2022. ed, ed. C. Boccato, et al. 2022: Springer International Publishing : Imprint: Springer, Cham.
22. Velu, R., et al., *A comprehensive review on bio-nanomaterials for medical implants and feasibility studies on fabrication of such implants by additive manufacturing technique*. Materials, 2020. **13**(1): p. 92.
23. AlMangour, B., et al., *Strengthening of stainless steel by titanium carbide addition and grain refinement during selective laser melting*. Materials Science and Engineering: A, 2018. **712**: p. 812-818.
24. Li, W., et al., *The combined influence of grain size distribution and dislocation density on hardness of interstitial free steel*. Journal of Materials Science & Technology, 2020. **45**: p. 35-43.
25. Sreeramagiri, P. and G. Balasubramanian, *Directed Energy Deposition of Multi-Principal Element Alloys*. Frontiers in Materials, 2022. **9**.

26. Aydogan, B., A. O'Neil, and H. Sahasrabudhe, *Microstructural and mechanical characterization of stainless steel 420 and Inconel 718 multi-material structures fabricated using laser directed energy deposition*. Journal of Manufacturing Processes, 2021. **68**: p. 1224-1235.
27. Pawawoi, I. Widiandyah, and D.H. Prajitno. *Synthesis oxide dispersion strengthening stainless steel doped with nano zirconia by mechanical alloying*. in *5th International Conference on Advances in Nuclear Science and Engineering, ICANSE 2015, November 18, 2015 - November 20, 2015*. 2017. Bandung, Indonesia: IOP Publishing Ltd.
28. Zhong, Y., et al., *Oxide dispersion strengthened stainless steel 316L with superior strength and ductility by selective laser melting*. Journal of Materials Science & Technology, 2020. **42**: p. 97-105.
29. Yan, F., et al., *Characterization of nano-scale oxides in austenitic stainless steel processed by powder bed fusion*. Scripta Materialia, 2018. **155**: p. 104-108.
30. Dai, C., *Oxide Dispersion Techniques for 316L Stainless Steel*. 2015, University of California, Davis: Ann Arbor. p. 133.
31. Davis, T.M., *Feasibility and Impact of Liquid/Liquid-encased dopants as method of composition control in Laser Powder Bed Fusion*. ScholarsArchive, 2021.
32. Paul, B.K., et al., *Oxide dispersion strengthened 304 L stainless steel produced by ink jetting and laser powder bed fusion*. CIRP Annals, 2020. **69**(1): p. 193-196.
33. Yu, W., et al., *Influence of re-melting on surface roughness and porosity of AlSi10Mg parts fabricated by selective laser melting*. Journal of Alloys and Compounds, 2019. **792**: p. 574-581.
34. Hanemann, T., et al., *Dimensionless Enthalpy as Characteristic Factor for Process Control in Laser Powder Bed Fusion*. Journal of Laser Micro Nanoengineering, 2020. **15**(3): p. 257-266.
35. Matthews, M.J., et al., *Denudation of metal powder layers in laser powder bed fusion processes*. Acta Materialia, 2016. **114**: p. 33-42.
36. Schneider, C.A., W.S. Rasband, and K.W. Eliceiri, *NIH Image to ImageJ: 25 years of image analysis*. Nature Methods, 2012. **9**(7): p. 671-675.
37. Larimian, T., et al., *Effect of energy density and scanning strategy on densification, microstructure and mechanical properties of 316L stainless steel processed via selective laser melting*. Materials Science and Engineering: A, 2020. **770**: p. 138455.
38. Aqilah, D.N., et al., *Effects of process parameters on the surface roughness of stainless steel 316L parts produced by selective laser melting*. Journal of Testing and Evaluation, 2018. **46**(4): p. 1673-1683.
39. Ziri, S., A. Hor, and C. Mabru, *Combined effect of powder properties and process parameters on the density of 316L stainless steel obtained by laser powder bed fusion*. International Journal of Advanced Manufacturing Technology, 2022. **120**(9-10): p. 6187-6204.
40. Du, Y., et al., *Study on improving wettability between nano ZrO<sub>2</sub> particles and liquid steel based on high energy ball mill*. Materials Letters, 2022. **314**.
41. Lee, J., S.Y. Kwon, and I.-H. Jung, *Phase diagram study and thermodynamic assessment of the Na<sub>2</sub>O-ZrO<sub>2</sub> system*. Journal of the European Ceramic Society, 2021. **41**(15): p. 7946-7956.
42. Bandriyana, B., et al. *Synthesis and microstructure evaluation of ODS steel 316L with zirconia dispersion*. in *5th International Conference on Advanced Material for Better*

- Future 2020, ICAMBF 2020, October 13, 2020 - October 14, 2020.* 2021. Surakarta, Indonesia: IOP Publishing Ltd.
43. AlMangour, B., et al., *Novel TiB<sub>2</sub>-reinforced 316L stainless steel nanocomposites with excellent room- and high-temperature yield strength developed by additive manufacturing.* Composites Part B: Engineering, 2019. **156**: p. 51-63.
  44. Han, Y., et al., *Selective laser melting of low-content graphene nanoplatelets reinforced 316L austenitic stainless steel matrix: Strength enhancement without affecting ductility.* Additive Manufacturing, 2020. **34**: p. 101381.
  45. Chen, X., et al., *Effect of nanoparticles formed in liquid melt on microstructure and mechanical property of high strength naval steel.* Journal of Materials Processing Technology, 2015. **222**: p. 224-233.
  46. Nayak, S.K., et al. *Effect of laser energy density on bulk properties of SS 316L structures built by laser additive manufacturing using powder bed fusion.* in *ASME 2019 Gas Turbine India Conference, GTINDIA 2019, December 5, 2019 - December 6, 2019.* 2019. Chennai, Tamil Nadu, India: American Society of Mechanical Engineers (ASME).
  47. Wang, Y., et al., *Microstructure and mechanical properties of TiN particles strengthened 316L steel prepared by laser melting deposition process.* Materials Science and Engineering: A, 2021. **814**: p. 141220.
  48. Chao, L., et al., *Analysis of Mechanical Properties and Permeability of Trabecular-Like Porous Scaffold by Additive Manufacturing.* Frontiers in Bioengineering and Biotechnology, 2021. **9**.
  49. Coulter, F.B., et al., *Additive Manufacturing of Multi-Scale Porous Soft Tissue Implants That Encourage Vascularization and Tissue Ingrowth.* Advanced Healthcare Materials, 2021. **10**(14).
  50. Novak, P., et al. *Powder metallurgy preparation of porous titanium for medical implants.* in *22nd International Conference on Metallurgy and Materials, METAL 2013, May 15, 2013 - May 17, 2013.* 2013. Brno, Czech republic: TANGER Ltd.
  51. Jiao, C., et al., *Additive manufacturing of Bio-inspired ceramic bone Scaffolds: Structural Design, mechanical properties and biocompatibility.* Materials and Design, 2022. **217**.
  52. Kwak, T.Y., et al., *Additive manufacturing of a porous titanium layer structure Ti on a Co-Cr alloy for manufacturing cementless implants.* Journal of Materials Research and Technology, 2021. **10**: p. 250-267.
  53. Guo, X., et al., *Corrosion resistance of candidate cladding materials for supercritical water reactor.* Annals of Nuclear Energy, 2019. **127**: p. 351-363.